

The stable XFEM for two-phase flows

Henning Sauerland^{a,*}, Thomas-Peter Fries^a

^a*Chair for Computational Analysis of Technical Systems, Center for Computational Engineering Science (CCES), RWTH Aachen University, Schinkelstr. 2, 52062 Aachen, Germany*

Abstract

The extended finite element method (XFEM) is frequently used in order to incorporate discontinuous solution properties into the approximation space. Discontinuities inside elements, as they *e.g.* occur in two-phase/free-surface flows with implicit interface descriptions, can thereby be accounted for appropriately. Yet, the XFEM is often prone to ill-conditioning of the global system matrix which reduces the performance of iterative solution techniques significantly. This paper introduces and studies new approaches to circumvent the problem of ill-conditioning with the XFEM. The stable XFEM, a recently proposed approach, is employed and studied in this work. Approximation properties and iterative solver performance are systematically compared for the different approaches which should improve the conditioning. Two recommended settings are finally used to solve a 3D free-surface flow benchmark problem and a classical two-phase flow problem. To our best knowledge, this is the first time that the stable XFEM is applied to industrially relevant flow problems.

Keywords: extended finite element method, XFEM, stable GFEM, two-phase flows, free-surface flows, enrichment, iterative solver

1. Introduction

The development of numerical schemes for the accurate simulation of two-phase flows is an active topic in the computational mechanics community.

*Corresponding author

Email addresses: sauerland@cats.rwth-aachen.de (Henning Sauerland),
fries@cats.rwth-aachen.de (Thomas-Peter Fries)

This research area is driven by the wide area of applications on one side and the technical complexity on the other side. Typical applications can be found in bubble column reactors, hydraulic design of dams, ship hydrodynamics, ink-jet printing or film coating. An accurate and flexible simulation tool for immiscible two-phase flow problems requires: (i) a robust description of the interface allowing for topological changes and (ii) appropriate accounting for the discontinuities in the material parameters and the field quantities, occurring across the interface.

In case of large interface deformations, an implicit interface description (interface-capturing) is usually preferred over a mesh based approach (interface-tracking). The level-set or volume of fluid (VOF) method are the most common interface-capturing methods [1, 2]. Here, an auxiliary field is used for the description of the moving interface. These approaches provide no topological restrictions on the interface motion, in contrast to typical interface-tracking methods [3] where the mesh has to follow the interface motion. However, the discontinuities across the interface require a special treatment when interface-capturing is used. As the discontinuities generally occur inside elements, standard finite element shape functions can not account for the discontinuous solution. So-called diffuse interface methods [1] overcome this difficulty by regularizing the discontinuities. In this work, however, we concentrate on the *sharp* treatment of the discontinuities.

Sharp interface methods rely on the modification of shape functions [4] or the enrichment of the approximation space, in order to account for inner element discontinuities. The extended finite element method (XFEM) [5, 6], applied in this work, employs such an enrichment approach. In the context of fluid mechanics, applications of the XFEM or similar enrichment approaches can, for example, be found in [7, 8, 9, 10, 11, 12, 13, 14, 15]. While it can be shown that the XFEM provides optimal approximation properties for discontinuous solutions, issues are observed when iterative solvers are applied. It is a well known drawback of the XFEM that it may lead to ill-conditioned system matrices [16], specifically, if the ratio of the volumes on both sides of the interface is large in cut elements. As the convergence properties of iterative solvers often depend on the condition number of the problem, a straightforward application of general purpose iterative solvers to an XFEM problem may fail. A recently proposed solution is the stable GFEM/XFEM [17]. Babuška and Banerjee introduce an enrichment which should lead to a conditioning not worse than that of the standard FEM, while promising the same convergence properties as the XFEM. In [18], a modified XFEM

space is introduced by neglecting (blocking) enrichment degrees of freedom (DOF) that are associated with very small supports, thus causing the ill-conditioning. If the criteria for the selection of neglectable DOFs is chosen carefully, the accuracy is not affected by this procedure. Another possibility is to apply special preconditioners in the solution phase. Béchet *et al.* [19] use a preconditioner based on local Cholesky decompositions and Menk and Bordas [20] apply a preconditioner evolving from a domain decomposition procedure. Both approaches lead to well-conditioned XFEM problems, while requiring additional matrix operations. In the context of two-phase flows, it is shown in [18] that diagonal scaling of the XFEM pressure mass matrix in the Schur complement preconditioner leads to a robust approach. A completely different approach is used in [21]. There, the nodes of elements containing the interface are moved in order to obtain more homogeneous ratios of the volumes on both sides of the interface and consequently improve the conditioning.

In this work, we study the issue of ill-conditioning in the XFEM for two-phase flows, concentrating on the stable XFEM and the application of iterative solvers. We also introduce a new criterion for the determination of degrees of freedom to be neglected and apply diagonal scaling in a more general manner. Convergence properties, condition numbers and iteration counts for the stable XFEM are compared to standard XFEM with diagonal scaling and the new blocking criterion, respectively. We also take a closer look at the approximation properties of the stable XFEM for steady two-phase flow problems. Finally, the stable XFEM is applied to industrially relevant two-phase/free-surface flow problems for the first time.

The paper is structured as follows. The governing equations and the discretization are introduced in Section 2. Section 3 introduces the XFEM approximation space. Subsequently, the issue of ill-conditioning and solution approaches are discussed in Section 4. The numerical examples in Section 5 show the effect of the previously introduced approaches on the convergence order and the performance of the iterative solver. This section is closed with two 3D validation problems. Final conclusions are drawn in Section 6.

2. Governing equations and discretization

Let Ω be the computational domain and Γ its boundary. In this work, the separation of Ω into two fluid phases is defined by means of the level-set method (Fig. 1). The scalar level-set function ϕ has a positive sign in one

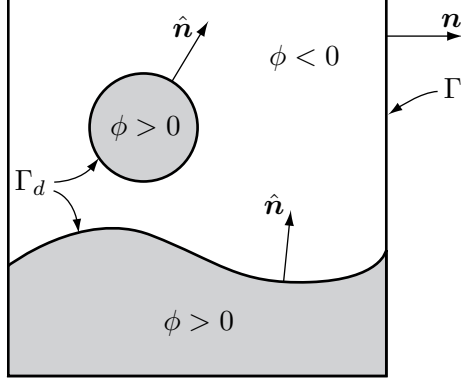


Figure 1: Computational domain.

phase and a negative sign in the other. By definition the interface between the two phases is given by

$$\Gamma_d = \{\mathbf{x} \in \Omega \mid \phi(\mathbf{x}, t) = 0\}, \quad (1)$$

while ϕ is usually defined as a signed-distance function:

$$\phi(\mathbf{x}, t) = \pm \min_{\mathbf{x}^* \in \Gamma_d(t)} \|\mathbf{x} - \mathbf{x}^*\|, \quad \forall \mathbf{x} \in \Omega. \quad (2)$$

The fluid velocity $\mathbf{u}(\mathbf{x}, t)$ and pressure $p(\mathbf{x}, t)$ of the two-phase flow problem is governed by the incompressible and isothermal Navier-Stokes equations:

$$\begin{aligned} \rho \left(\frac{\partial \mathbf{u}}{\partial t} + \mathbf{u} \cdot \nabla \mathbf{u} - \mathbf{f} \right) - \nabla \cdot \boldsymbol{\sigma} &= 0 \quad \text{in } \Omega \times [0, T], \\ \nabla \cdot \mathbf{u} &= 0 \quad \text{in } \Omega \times [0, T], \end{aligned} \quad (3)$$

with

$$\rho(\phi) = \begin{cases} \rho_1, & \phi(\mathbf{x}, t) < 0, \\ \rho_2, & \phi(\mathbf{x}, t) > 0, \end{cases} \quad (4)$$

being the density of the respective fluid phase and \mathbf{f} the body force (gravity). The stress tensor $\boldsymbol{\sigma}$ is given by

$$\boldsymbol{\sigma} = -p\mathbf{I} + 2\mu\boldsymbol{\varepsilon}(\mathbf{u}) \quad \text{with} \quad \boldsymbol{\varepsilon}(\mathbf{u}) = \frac{1}{2} \left(\nabla \mathbf{u} + (\nabla \mathbf{u})^T \right), \quad (5)$$

where

$$\mu(\phi) = \begin{cases} \mu_1, & \phi(\mathbf{x}, t) < 0, \\ \mu_2, & \phi(\mathbf{x}, t) > 0, \end{cases} \quad (6)$$

is the corresponding dynamic viscosity and \mathbf{I} the identity tensor. The Dirichlet and Neumann boundary condition are

$$\mathbf{u} = \hat{\mathbf{u}} \quad \text{on } \Gamma_u \times [0, T], \quad (7)$$

$$\mathbf{n} \cdot \boldsymbol{\sigma} = \hat{\mathbf{h}} \quad \text{on } \Gamma_h \times [0, T]. \quad (8)$$

Γ_u and Γ_h denote the Dirichlet and Neumann part of the boundary. At the interface the following conditions are prescribed

$$[\mathbf{u}]_{\Gamma_d} = \mathbf{0} \quad \text{on } \Gamma_d(t) \times [0, T], \quad (9)$$

$$[\hat{\mathbf{n}} \cdot \boldsymbol{\sigma}]_{\Gamma_d} = \gamma \kappa \hat{\mathbf{n}} \quad \text{on } \Gamma_d(t) \times [0, T]. \quad (10)$$

γ is the surface tension coefficient, κ the interface curvature and $[f]_{\Gamma_d}$ defines the jump of f across the interface. A divergence free initial velocity field closes the problem:

$$\mathbf{u}(\mathbf{x}, 0) = \hat{\mathbf{u}}_0(\mathbf{x}) \quad \text{in } \Omega. \quad (11)$$

In order to account for the interface movement, the level-set transport equation

$$\frac{\partial \phi}{\partial t} + \mathbf{u}(\mathbf{x}, t) \cdot \nabla \phi = 0 \quad \text{in } \Omega \times [0, T] \quad (12)$$

is solved, with $\mathbf{u}(\mathbf{x}, t)$ being the velocity field obtained from the Navier-Stokes equations (3) and

$$\phi(\mathbf{x}, 0) = \hat{\phi}_0(\mathbf{x}) \quad \text{in } \Omega \quad (13)$$

is the initial level-set function. Frequent reinitialization of the level-set field is necessary in order to prevent the development of high gradients in ϕ and to maintain the signed-distance property. It is well-known that the level-set method is not mass-conserving. *Global* mass conservation is enforced by using the iterative approach described in [22].

Eqs. (3) and (12) are discretized in time using a second order Crank-Nicolson scheme. Writing the Navier-Stokes equations (3) as

$$\frac{\partial \mathbf{u}}{\partial t} = F(\mathbf{u}, t), \quad (14)$$

this time discretization leads to

$$\frac{\mathbf{u}^{n+1} - \mathbf{u}^n}{\Delta t} = \theta \cdot F(\mathbf{u}^{n+1}, t^{n+1}) + (1 - \theta) \cdot F(\mathbf{u}^n, t^n), \quad \theta = \frac{1}{2}, \quad (15)$$

(analogously for the level-set transport (12)) whereas the pressure and the continuity equation are treated fully implicitly. See [23] for details on time integration within the XFEM. For brevity, the time discretization (15) will not be included in the following weak formulations.

The spatial discretization is carried out using bilinear quadrilateral or trilinear hexahedral finite elements. Assuming suitable test and trial spaces, the SUPG/PSPG/LSIC-stabilized weak formulation of (3) follows to: Find $\mathbf{u}^h \in \mathcal{S}_u^h$ and $p^h \in \mathcal{S}_p^h$ such that $\forall \mathbf{w}^h \in \mathcal{V}_u^h, \forall q^h \in \mathcal{V}_p^h$:

$$\begin{aligned} & \int_{\Omega} \mathbf{w}^h \cdot \rho \left(\frac{\partial \mathbf{u}^h}{\partial t} + \mathbf{u}^h \cdot \nabla \mathbf{u}^h - \mathbf{f} \right) d\Omega + \int_{\Omega} \boldsymbol{\varepsilon}(\mathbf{w}^h) : \boldsymbol{\sigma}(\mathbf{u}^h, p^h) d\Omega \\ & + \int_{\Omega} q^h \nabla \cdot \mathbf{u}^h d\Omega + \sum_{e=1}^{n_{el}} \int_{\Omega_{el}^e} \tau_s \left(\mathbf{u}^h \cdot \nabla \mathbf{w}^h + \frac{1}{\rho} \nabla q^h \right) \cdot \\ & \quad \left[\rho \left(\frac{\partial \mathbf{u}^h}{\partial t} + \mathbf{u}^h \cdot \nabla \mathbf{u}^h - \mathbf{f} \right) - \nabla \cdot \boldsymbol{\sigma}(\mathbf{u}^h, p^h) \right] d\Omega \quad (16) \\ & + \sum_{e=1}^{n_{el}} \int_{\Omega_{el}^e} \tau_{LSIC} \nabla \cdot \mathbf{w}^h \rho \nabla \cdot \mathbf{u}^h d\Omega \\ & = \int_{\Gamma_h} \mathbf{w}^h \cdot \hat{\mathbf{h}} d\Gamma + \int_{\Gamma_d} \gamma \kappa \mathbf{w}^h \cdot \hat{\mathbf{n}} d\Gamma, \end{aligned}$$

with n_{el} being the number of elements and $\boldsymbol{\varepsilon}$ and $\boldsymbol{\sigma}$ defined in Eq. (5). The force term is assumed to be stationary and constant. The stabilization parameter τ_s is chosen according to [24]:

$$\tau_s = \left[\left(\frac{2}{\Delta t} \right)^2 + \left(\frac{2|\mathbf{u}^h|_2}{h_e} \right)^2 + \left(\frac{4\nu}{h_e^2} \right)^2 \right]^{-\frac{1}{2}} \quad (17)$$

where $\nu = \mu/\rho$ is the kinematic viscosity and h_e is the element length (see *e.g.* [25] for details). For high Reynolds number flows, the following LSIC (least-squares on incompressibility constraint) stabilization parameter [26] is employed:

$$\tau_{\text{LSIC}} = \frac{h_e}{2} |\mathbf{u}^h|_2 z, \quad z = \begin{cases} \frac{\text{Re}_e}{3}, & \text{Re}_e \leq 3, \\ 1, & \text{Re}_e > 3, \end{cases} \quad \text{Re}_e = \frac{h_e |\mathbf{u}^h|_2}{2\nu}. \quad (18)$$

Due to the convective type of the level-set transport equation (12), the SUPG stabilization is applied here, too. The weak formulation is then defined as: Find $\phi^h \in \mathcal{S}_\phi^h$ such that $\forall \mathbf{w}^h \in \mathcal{V}_\phi^h$:

$$\begin{aligned} & \int_{\Omega} \mathbf{w}^h \cdot \left(\frac{\partial \phi^h}{\partial t} + \mathbf{u}^h \cdot \nabla \phi^h \right) d\Omega \\ & + \sum_{e=1}^{n_{\text{el}}} \int_{\Omega_{el}^e} \tau_s (\mathbf{u}^h \cdot \nabla \mathbf{w}^h) \cdot \left(\frac{\partial \phi^h}{\partial t} + \mathbf{u}^h \cdot \nabla \phi^h \right) d\Omega = 0. \end{aligned} \quad (19)$$

The stabilization parameter τ_s is given by (17) with $\nu = 0$.

We want to underline the strongly coupled nature of (16) and (19). There is a mutual influence of the level-set function ϕ and the fluid velocity field. For the latter, the non-linear Navier-Stokes equations are solved in series of Picard iterations.

3. XFEM approximation space

In two-phase flows, due to the density and viscosity differences, discontinuities in the pressure and velocity field exist across the interface [27]. Appropriately accounting for this situation is inevitable for an accurate numerical description of such flow phenomena [28]. As a cause of the implicit interface description, the named discontinuities occur inside elements in this work. In the framework of the XFEM, the test and trial spaces are locally enriched with discontinuous functions to accurately account for discontinuous solutions. In [15], we showed that it is sufficient and advisable to only enrich the pressure approximation space for the considered two-phase flow problems. The pressure approximation is then

$$p^h(\mathbf{x}, t) = \underbrace{\sum_{i \in I} N_i(\mathbf{x}) p_i}_{\text{strd. FE approx.}} + \underbrace{\sum_{i \in I^*} M_i(\mathbf{x}, t) a_i}_{\text{enrichment}}. \quad (20)$$

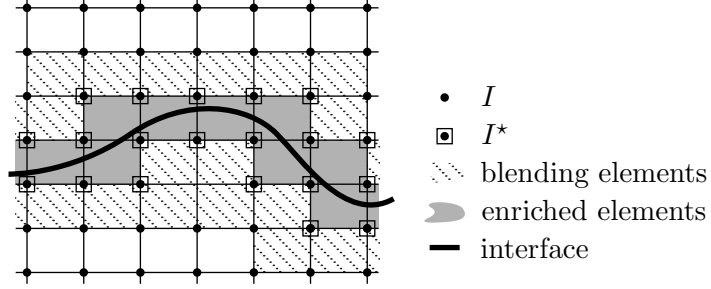


Figure 2: Enriched domain.

$N_i(\mathbf{x})$ is the standard FE shape function for node i , I is the set of all nodes in the domain, $M_i(\mathbf{x}, t)$ are the local enrichment functions, p_i are the nodal pressure values, a_i are the additional XFEM unknowns, and I^* is the nodal subset of the enrichment (*cf.* Fig. 2). In order to ensure the Kronecker- δ property of the overall approximation (20), $M_i(\mathbf{x}, t)$ is further specified as follows [29]:

$$M_i(\mathbf{x}, t) = N_i(\mathbf{x}) \cdot [\psi(\mathbf{x}, t) - \psi(\mathbf{x}_i, t)] \quad \forall i \in I^*, \quad (21)$$

with $\psi(\mathbf{x}, t)$ being the global enrichment function. Based on our findings in [15], we chose the sign-enrichment

$$\psi(\mathbf{x}, t) = \text{sign}(\phi(\mathbf{x}, t)) = \begin{cases} -1, & \phi(\mathbf{x}, t) < 0, \\ 0, & \phi(\mathbf{x}, t) = 0, \\ 1, & \phi(\mathbf{x}, t) > 0, \end{cases} \quad (22)$$

irrespective of the fact whether a kink or a jump exists in the pressure field. Issues with so-called blending elements (*cf.* Fig. 2) are prevented with this enrichment function [30, 31].

It should be noted that the quadrature of the weak form (16) requires special consideration when using the XFEM. The used approximation spaces are enriched with discontinuous functions and the density and viscosity are discontinuous, too. Therefore, some of the integrands in the weak formulations are discontinuous as well. However, standard Gauss quadrature requires smoothness of the integrands. In order to obtain an accurate numerical quadrature, the cut elements are subdivided for integration purposes such that they align with the interface. Standard Gauss rules can then be applied in the subelements, resulting from the decomposition. For details we refer *e.g.* to [5, 6].

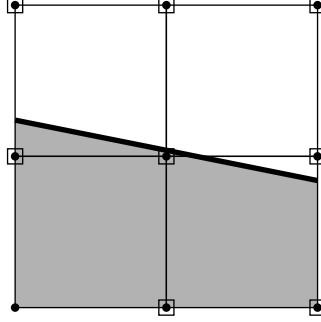


Figure 3: Exemplary mesh and interface. Enriched nodes are surrounded by a square.

4. Iterative solvers with the XFEM

In our parallel flow solver framework, typically a LGMRES Krylov subspace method is used in combination with an Additive Schwarz Method (ASM) preconditioner, both provided by the PETSc suite [32]. A common disadvantage of XFEM formulations is the typically ill-conditioned system matrix [16]. Enrichment functions with very small support are the cause of this XFEM related ill-conditioning. Hence, a straightforward application of iterative solvers to an XFEM problem will generally not be of success as the rate of convergence of most iterative solvers often depends on the condition number of the underlying system matrix [33].

In order to get an idea of the order of magnitude of the condition number, we consider the mesh in Fig. 3 with the depicted interface. Building the global XFEM system matrix \mathbf{K} using formulation (16) with $\rho_1 = \rho_2 = 1.0 \text{ kg/m}^3$ and $\mu_1 = \mu_2 = 1.0 \text{ kg/m/s}$, let $\lambda_{\min}(\mathbf{K})$ and $\lambda_{\max}(\mathbf{K})$ be the extreme eigenvalues of \mathbf{K} . The spectral condition number [33] computes to

$$\kappa(\mathbf{K}) = \left| \frac{\lambda_{\max}(\mathbf{K})}{\lambda_{\min}(\mathbf{K})} \right|. \quad (23)$$

Table 1 shows the condition numbers of the standard FEM system matrix and our XFEM matrix for the given mesh and the governing equations shown above. Here, the condition number for the XFEM problem exceeds the standard FEM problem by 3 orders of magnitude. Furthermore, upon mesh refinement, it can be shown that the condition number increases dramatically larger for the XFEM matrix as for the FEM matrix [17]. Hence, a standard approach with preconditioned iterative solvers is most likely to fail. In the following, solutions to this problem are reviewed.

Case	$\kappa(\mathbf{K})$
FEM	15
XFEM	66581

Table 1: Spectral condition numbers of the system matrix \mathbf{K} for the mesh in Fig. 3.

Remark Another disadvantage from the viewpoint of performance is the time dependent approximation space in the XFEM. The additional XFEM degrees of freedom travel with the interface, that is, a varying number of degrees of freedom per node exists over time. Consequently, the non-zero structure of the system matrix has to be updated in every iteration, leading to an overhead compared to the standard FEM.

4.1. Blocking of degrees of freedom

It is often useful to remove enrichment functions with very small support, which lead to a large condition number of the resulting XFEM system matrix. Reusken [18] introduced a modified XFEM space, excluding such enrichments while maintaining optimal convergence rates. The enrichments to be blocked are identified on shape function level. We propose a geometrically motivated criterion. Let A_1^e and A_2^e be the area/volume of the two phases occupied in a cut element e . Initially, all nodes of elements containing the interface (*i.e.* the enriched nodes) are tagged **block**. During the assembly step the following procedure is performed for each element:

1. If, for the element under consideration,

$$\frac{\min(A_1^e, A_2^e)}{\max(A_1^e, A_2^e)} < C_{\text{block}}, \quad (24)$$

holds for a user-specified constant $C_{\text{block}} \ll 1$, proceed with the next step, otherwise all element nodes are tagged **save** and the next step is skipped.

2. Mark all element nodes as **save** whose algebraic sign of the level-set value is the same as that of the phase occupying the smaller volume in this element. Note that the **save** tag may overwrite the **block** tag that a node obtained initially. Hereby, it is ensured that enrichments are only blocked if they have small supports in *all* cut elements they belong to.

After all cut elements are processed, ‘remove’ the enrichment degrees of freedom of the nodes i marked as **block** by enforcing a Dirichlet boundary condition for the XFEM unknown

$$a_i = 0. \quad (25)$$

Reconsidering the toy mesh of Fig. 3, we apply the procedure above with $C_{\text{block}} = 0.01$. As a result, the condition number of the XFEM matrix is decreased by one order of magnitude, $\kappa(\mathbf{K}) \approx 6129$, while the enrichment of the upper right node is removed. It should be emphasized that too large C_{block} may influence the favorable approximation properties of the XFEM. The effect of the blocking on the approximation properties is studied in Section 5.

4.2. Additional preconditioning

It is common practice to use iterative solvers in conjunction with preconditioners, in order to improve convergence rates of the iterative solvers. In addition, one could think of applying an *additional* preconditioner tailored to the specific needs of the XFEM. Béchet *et al.* [19] developed a preconditioner for crack propagation with XFEM, based on a local Cholesky decomposition. Menk and Bordas [20] apply a preconditioner evolving from a domain decomposition procedure. Both approaches are able to bound the condition number almost independent of the mesh size.

For the two-phase flow problems, we consider a diagonal scaling (Jacobi preconditioner) [34] of the linear system

$$\mathbf{D}^{-1/2} \mathbf{K} \mathbf{D}^{-1/2} (\mathbf{D}^{1/2} \mathbf{x}) = \mathbf{D}^{-1/2} \mathbf{b}, \quad \text{with } \mathbf{D} = \text{diag}(\mathbf{K}).$$

In [18], the diagonal scaling is applied to the enriched pressure mass matrix in the Schur complement preconditioner only. It is shown that the condition number of the scaled pressure mass matrix is independent of the mesh size. Because of implementational reasons, we do not use block preconditioning and apply diagonal scaling to the complete system matrix. In this case, no boundedness of the condition number of the *complete* system matrix could be observed. However, if the diagonal scaling is applied to the XFEM system matrix for Fig. 3, the condition number reduces significantly to $\kappa(\mathbf{K}) \approx 33$ —the same order of magnitude as for the standard FEM. In contrast to the blocking approach, all enrichment DOFs are preserved. Again, we underline that the diagonal scaling is applied *in addition* to the general purpose preconditioners.

4.3. Stable XFEM

Recently, Babuška and Banerjee [17] proposed the stable GFEM/XFEM with a modified step enrichment. It is claimed to offer the same convergence properties as the standard step enrichment, while the conditioning remains in the range of the standard FEM. Instead of (21), the local enrichment function in the stable XFEM (sXFEM) is defined as

$$M_i^{\star, \text{stable}}(\mathbf{x}, t) = N_i(\mathbf{x}) \cdot [\psi(\mathbf{x}, t) - \mathcal{I}_{\psi_i}(\mathbf{x})] \quad \forall i \in I^{\star}, \quad (26)$$

with

$$\mathcal{I}_{\psi_i}(\mathbf{x}) = \sum_{i \in I^{\star}} N_i(\mathbf{x}) \cdot \psi(\mathbf{x}_i, t) \quad (27)$$

being the linear interpolant of the global enrichment function in the cut elements. Our test problem with sXFEM leads to $\kappa(\mathbf{K}) \approx 514$. The condition number is not of the same order as for the FEM, but much lower compared to standard XFEM. Furthermore, it can be shown, that the change of the condition number upon mesh refinement is of the same rate for the sXFEM than for the XFEM [17]. A comparison of the convergence properties of sXFEM follows in the next Section.

Remark $M_i^{\star, \text{stable}}$ is a quadratic term (*cf.* (26), (27)). This has to be considered in the choice of the integration scheme.

5. Numerical examples

5.1. Stationary test cases

The following stationary test cases serve as the purpose to compare the approaches proposed in Section 4 with respect to the spatial accuracy and iteration counts, respectively. All test cases in this subsection are evaluated using the stationary Navier-Stokes equations.

5.1.1. Circular interface

First of all, a static circular interface in a square domain is considered (*cf.* Fig. 4). The radius of the circle is chosen as $r = 0.5$ m. Viscosity and density are equal in both phases: $\rho_1 = \rho_2 = 1.0 \text{ kg/m}^3$, $\mu_1 = \mu_2 = 1.0 \text{ kg/m/s}$. Volume forces are neglected, while a constant unit force is applied at the interface. Using the *analytical* curvature and analytical normal vectors of the

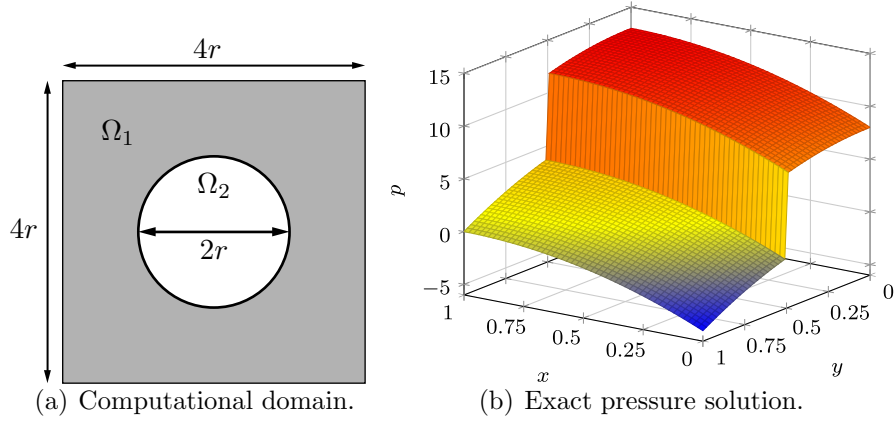


Figure 4: Static circular interface.

circular interface, this corresponds to the usage of the surface tension term in Eq. (16) with $\gamma = 1.0 \text{ kg/s}^2$. According to the Laplace-Young equation, the exact solution to this problem is

$$\mathbf{u}(\mathbf{x}) = \mathbf{0}, \quad (28)$$

$$p(\mathbf{x}) = \begin{cases} 0, & \mathbf{x} \in \Omega_1, \\ \gamma \cdot \kappa, & \mathbf{x} \in \Omega_2, \end{cases} \quad (29)$$

(*cf.* Fig. 4). No-slip boundary conditions are applied at all boundaries and a reference pressure of $p = 0 \text{ N/m}^2$ is prescribed at one corner.

Table 2 presents the pressure error in the L^2 -norm for the approaches introduced in Section 4 and mesh sizes of $h = 1/40, 1/80$ and $1/160 \text{ m}$. Table 3 shows the required number of iterations until convergence to machine precision. Regarding the blocking of enrichment degrees of freedom, we observe that a larger blocking constant leads to larger pressure errors. This is reasonable as the XFEM approximation space essentially reduces to the standard FEM space for very large blocking constants. For $C_{\text{block}} = 0.001$, considerably less iterations are required compared to the standard XFEM case, while the convergence order is not affected. For the larger blocking constants, the pressure jump can not be accounted for appropriately anymore—the convergence order drops. The worse approximation properties weaken the increase in performance of the iterative solver due to the blocking, *i.e.* the iteration counts go up again for $C_{\text{block}} = 0.01$ and 0.1 (*cf.* Table 3). The diagonal scaling and sXFEM do not show an influence on the error. However, the per-

Case	$h = 1/40$	$h = 1/80$	$h = 1/160$	$\mathcal{O}(h^m)$
XFEM	2.636×10^{-4}	8.451×10^{-5}	3.186×10^{-5}	1.52
XFEM $C_{\text{block}} = 0.001$	2.636×10^{-4}	8.451×10^{-5}	3.186×10^{-5}	1.52
XFEM $C_{\text{block}} = 0.01$	2.655×10^{-4}	8.674×10^{-5}	3.498×10^{-5}	1.46
XFEM $C_{\text{block}} = 0.1$	1.220×10^{-3}	8.780×10^{-4}	4.810×10^{-4}	0.67
XFEM scaled	2.636×10^{-4}	8.451×10^{-5}	3.186×10^{-5}	1.52
sXFEM	2.636×10^{-4}	8.447×10^{-5}	3.188×10^{-5}	1.52
sXFEM scaled	2.636×10^{-4}	8.447×10^{-5}	3.188×10^{-5}	1.52

Table 2: Pressure error in the L^2 -norm and convergence order for the static circular interface, evaluated with the approaches introduced in Section 4.

Case	$h = 1/40$	$h = 1/80$	$h = 1/160$
XFEM	453	976	2976
XFEM $C_{\text{block}} = 0.001$	167	589	2661
XFEM $C_{\text{block}} = 0.01$	172	682	2796
XFEM $C_{\text{block}} = 0.1$	172	833	2896
XFEM scaled	162	578	1746
sXFEM	176	747	2367
sXFEM scaled	158	537	1731

Table 3: Iteration counts for the static circular interface, evaluated with the approaches introduced in Section 4.

formance of the iterative solver increases significantly for both approaches. Using the sXFEM requires much less iterations compared to XFEM, but still slightly more than XFEM with diagonal scaling. sXFEM and XFEM with diagonal scaling lead to comparable iteration counts with sXFEM staying slightly ahead of the competition. Drawing an intermediate conclusion, diagonal scaling will be preferred over blocking of degrees of freedom in the following, if possible. In case of sXFEM, diagonal scaling is also useful to lower the iteration counts even more.

Remark We use the analytical curvature and analytical normal vectors of the circular interface in order to apply the surface tension force. However, due to the sub-cell quadrature, a piecewise linear interface approximation is obtained. This inconsistency leads to the suboptimal convergence rate of 1.52 in Table 2 (instead of the optimal rate of 2.0).

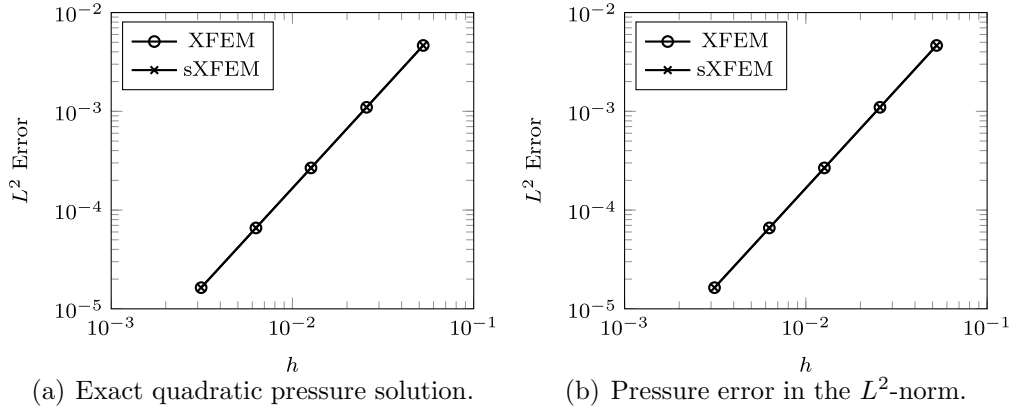


Figure 5: Straight interface: Jump in p .

5.1.2. Straight interface

In this section, we concentrate on the approximation properties of the stable XFEM. The following test case is proposed by Ausas *et al.* [35]. In contrast to the previous example, a straight interface is considered and the pressure jump is induced by a velocity field and a viscosity jump across the interface. We consider a square domain $\Omega \in [0, 1] \times [0, 1]$ with a horizontal interface at $y = 0.5$, $\rho = \rho_1 = \rho_2 = 10.0 \text{ kg/m}^3$, $\mu_1 = 5.0 \text{ kg/m/s}$ and $\mu_2 = 1.0 \text{ kg/m/s}$. Neglecting volume forces and prescribing the following linear velocity field

$$\mathbf{u}(\mathbf{x}) = \begin{pmatrix} 1 - x \\ y \end{pmatrix}, \quad (30)$$

the exact solution for the pressure field can be found to be

$$p(\mathbf{x}) = \begin{cases} \rho \left(x - \frac{1}{2}(x^2 + y^2) \right) + 2(\mu_1 - \mu_2), & y < 0.5, \\ \rho \left(x - \frac{1}{2}(x^2 + y^2) \right), & y > 0.5. \end{cases} \quad (31)$$

It is obvious that the quadratic pressure field (31) does not belong to either the XFEM or sXFEM approximation space, when bilinear elements are used.

The velocity field (30) is imposed at the boundaries and a reference pressure $p = 0 \text{ N/m}^2$ is prescribed at the upper right corner. We consider a series of successively refined quadrilateral meshes, with mesh sizes of $h = 1/19, 1/39, 1/79, 1/159$ and $1/319 \text{ m}$. Fig. 5 shows the exact pressure solution and a logarithmic plot of the pressure error in the L^2 -norm for the different

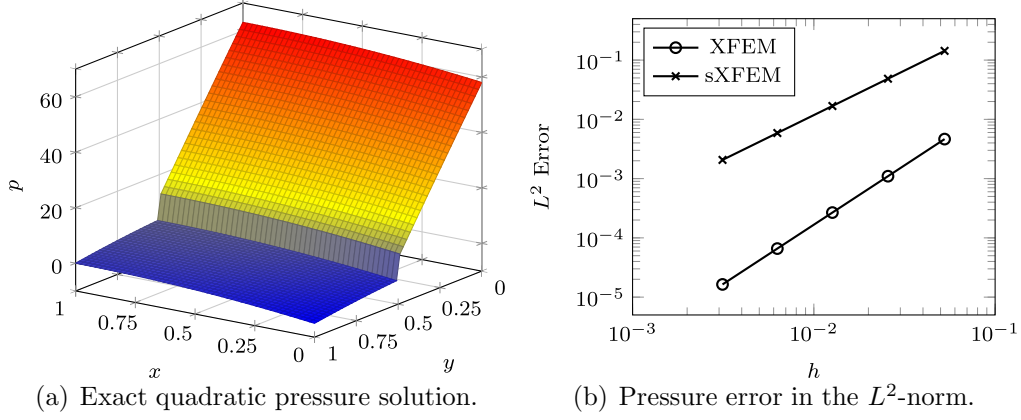


Figure 6: Straight interface: Jump in p and $\frac{dp}{dx}$.

meshes. XFEM and sXFEM lead to the same results showing a convergence order of $\mathcal{O}(h^2)$, as expected.

If a discontinuous volume force is applied in addition:

$$f_x = 0, f_y = \begin{cases} -10, & y < a, \\ 0, & y > a, \end{cases} \quad (32)$$

a jump in the pressure *and* in the pressure gradient exists. The exact solution for the pressure field is then given by

$$p(\mathbf{x}) = \begin{cases} \rho \left(x - \frac{1}{2}(x^2 + y^2) - f_y(a - y) \right) + 2(\mu_1 - \mu_2), & y < 0.5, \\ \rho \left(x - \frac{1}{2}(x^2 + y^2) \right), & y > 0.5. \end{cases} \quad (33)$$

Boundary conditions, interface position and the meshes are the same as in the previous case. Fig. 6 shows the exact pressure solution and a logarithmic plot of the pressure error in the L^2 -norm for the different meshes. The standard XFEM still obtains an optimal convergence rate. In contrast, sXFEM produces pressure errors orders of magnitude larger and a suboptimal convergence order of $\mathcal{O}(h^{\frac{3}{2}})$.

The last test case shows an important result: Unlike the standard XFEM, the stable XFEM is not able to account for jumps in the pressure *gradient* with optimal accuracy, when using the sign-enrichment. This finding still has to be investigated in more depth in the future, as well as the idea to apply an additional enrichment with sXFEM in order to account for jumps in the pressure gradient.

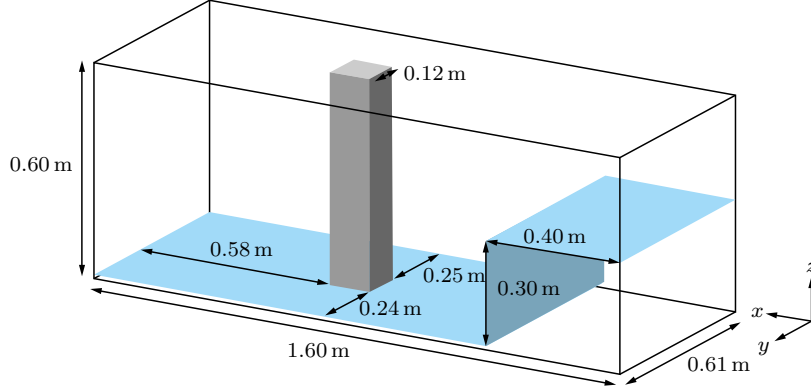


Figure 7: Dam breaking: Geometry and initial water surface.

5.2. Dam breaking benchmark

In the following benchmark test case, the XFEM and sXFEM are compared for an industrially relevant problem. The impact of a water wave on a tall coastal structure [36] is examined. Figure 7 depicts the geometry and the initial water surface. In the experimental setup, the water is initially contained behind a gate. We also take into account the thin layer of water (approximately 0.01 m) on the bottom of the tank, which could not be avoided in the experiments. The physical parameters are given by: $\rho_{\text{air}} = 1.225 \text{ kg/m}^3$, $\rho_{\text{water}} = 999.1 \text{ kg/m}^3$, $\mu_{\text{air}} = 0.0000178 \text{ kg/m/s}$, $\mu_{\text{water}} = 0.001137 \text{ kg/m/s}$, $\gamma_{\text{water}} = 0.0728 \text{ kg/s}^2$, and $f_z = -g = -9.81 \text{ m/s}^2$. In order to avoid the explicit computation of the interface curvature in the surface-tension term in Eq. (16), the Laplace-Beltrami approach is employed (see *e.g.* [15] and [37] for details). An adaptively refined hexahedral mesh is used, as described in [37], with a minimal element size of $h \approx 0.01525 \text{ m}$ around the interface and a time step of $\Delta t = 0.001 \text{ s}$. The structure is assumed to be infinitely stiff and slip conditions are applied on all boundaries.

Fig. 8 shows the water phase at different time instances. Due to gravity, the initial water column collapses and evolves into a wave moving towards the structure. Upon impact, the wave is separated by the structure and rides up its upstream face. Scarcely rejoined, the water is reflected at the upstream wall of the tank. Again, the now weakened waves impinge on the structure, this time from the downstream face. The wave front is once more reflected from the downstream wall of the tank, before the waves slowly decay.

The experimental data provided in [36] comprises time histories of the

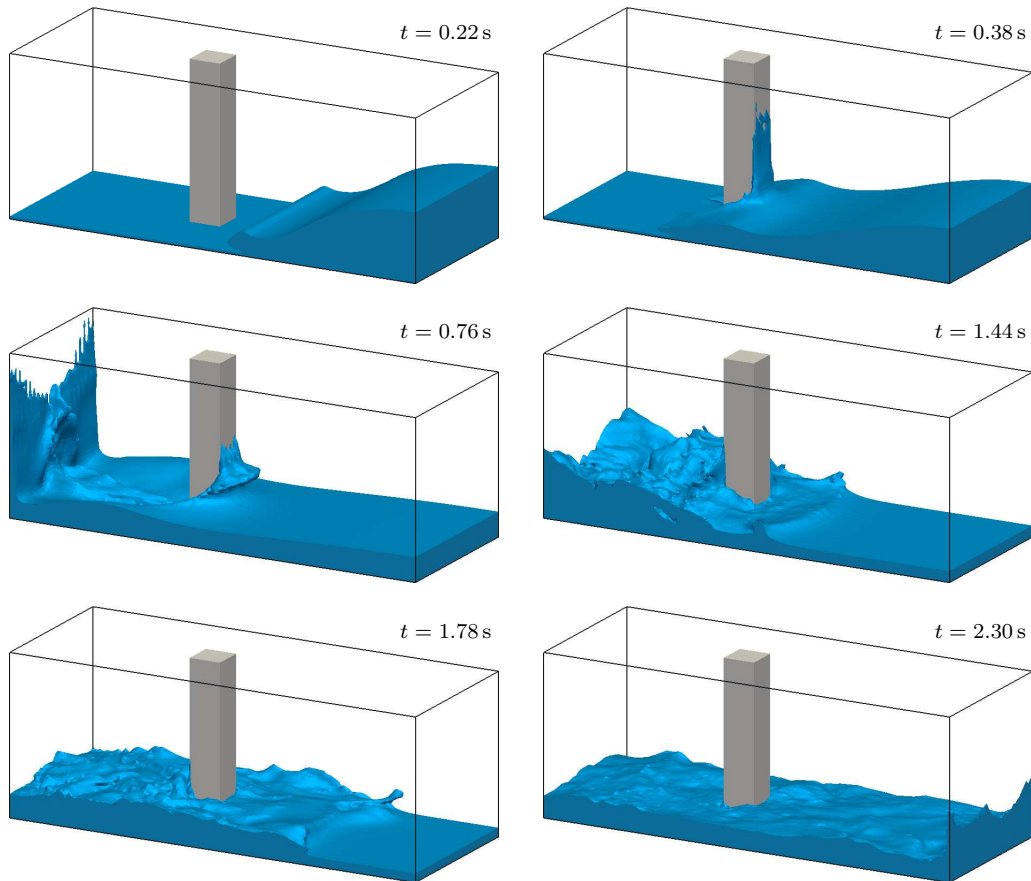


Figure 8: Dam breaking: Water phase at different time instances.

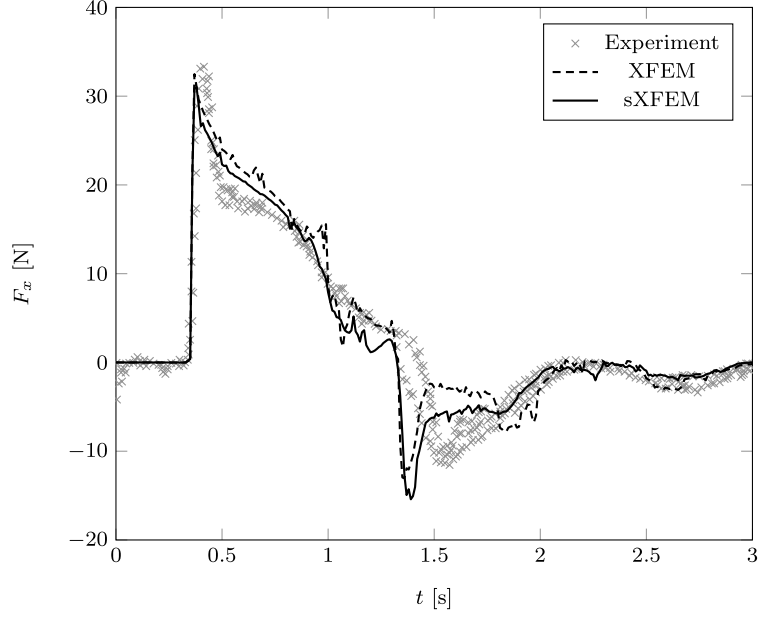


Figure 9: Dam breaking: Force in x -direction on the structure.

x -velocity of the water phase at a point 0.146 m upstream of the structure and 0.026 m off the floor and the overall force in x -direction acting on the structure. The data was obtained from four independent experiments. Both quantities for the stable XFEM and the standard XFEM are compared in Figs. 9 and 10. The plot of the force clearly shows the impact on the front ($t \approx 0.5$ s) and the back of the structure ($t \approx 1.5$ s). Altogether, the agreement of XFEM and sXFEM with the experiments is good. The only major difference lies in the overprediction of the force during the impact at the back of the structure, which also happens slightly earlier compared to the experiments (*cf.* Fig. 9, $t = 1.25$ - 1.75 s). The shift in time could be explained by the fact that the turbulent flow structures are underresolved—that is, not modeled. Accounting for turbulence more accurately, would most likely delay the wave after the violent collapse of the reflected water at the upstream face of the tank. The plot of the x -velocity also shows the largest deviations from the experiments between 1.25 and 1.75 s. However, the deviations are not that pronounced as for the force. The results of XFEM and sXFEM are qualitatively comparable.

While the differences in the above results of XFEM and sXFEM are small, the difference in performance for this test case is eminent. Using 32

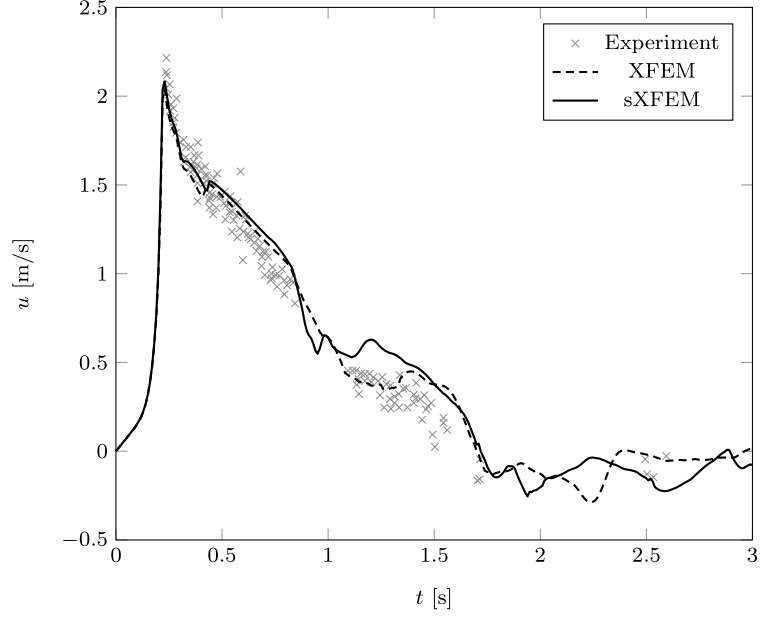


Figure 10: Dam breaking: x -velocity at coordinate $(0.754, 0.31, 0.026)$ m.

cores on an Intel Nehalem cluster, sXFEM achieves about 313 time steps per hour compared to about 200 time steps per hour with XFEM. It should be noted that blocking, with $C_{\text{block}} = 0.001$, was applied *in addition* to diagonal scaling for the XFEM. As the interface motion is severe and small droplets develop, the iterative solver had hard times converging even with blocking being enabled. sXFEM on the other side converged smoothly.

5.3. Rising droplets

Rising droplets belong to the classical two-phase flow problems with surface tension. The numerical prediction of the behavior of single droplets is for example important in the development of liquid-liquid extraction columns [38]. In the following, the rise velocity of n-butanol droplets in water is investigated. Therefore, five different droplet diameters are considered: $d = 1.0, 1.5, 2.0, 3.0$ and 4.0 mm. The computational domain occupies a rectangular box with the dimensions $7.5d \times 7.5d \times 15d$ and the center of the droplet is initially placed $2d$ off the bottom wall. The physical parameters are given by: $\rho_{\text{butanol}} = 845.422 \text{ kg/m}^3$, $\rho_{\text{water}} = 986.506 \text{ kg/m}^3$, $\mu_{\text{butanol}} = 0.003281 \text{ kg/m/s}$, $\mu_{\text{water}} = 0.001388 \text{ kg/m/s}$, $\gamma_{\text{butanol}} = 0.00163 \text{ kg/s}^2$, and $f_z = -g = -9.81 \text{ m/s}^2$. The minimal element size around the interface is

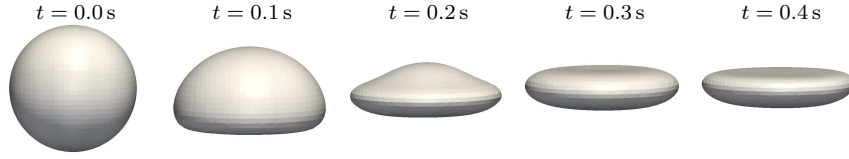


Figure 11: Rising droplet: Droplet shape at different time instances for $d = 4$ mm.

$h \approx 0.078125d$ and a time step of $\Delta t = 0.0005$ s is chosen. No-slip conditions are applied on all boundaries.

Fig. 11 exemplarily depicts the shape of the droplet with $d = 4$ mm over time, which is in very good agreement with the numerical results in [38]. For a more detailed comparison, the rise velocity of the droplets,

$$\mathbf{v}_{\text{rise}} = \frac{\int_{\Omega_{\text{drop}}} \mathbf{u}(\mathbf{x}, t) d\Omega}{\int_{\Omega_{\text{drop}}} 1 d\Omega}, \quad (34)$$

is considered. After some time (here: $t \approx 0.5$ s), \mathbf{v}_{rise} reaches a quasi-steady state. A steady sedimentation velocity $v_{\text{sed}} = \|\mathbf{v}_{\text{rise}}\|$ is determined for each droplet diameter and is compared with a model prediction and the experimental results given in [38], see Fig. 12. In this case, the results for XFEM and sXFEM are almost identical. Except for the two smallest droplets, the numerical sedimentation velocities are slightly lower than those of the experiment. We find that the blocking of enrichment DOFs for the standard XFEM is not as important as for the previous test case. In fact, even without blocking the iterative solver performs well with diagonal scaling only. We trace this back to the fact that the interface is much smoother in this case compared to the dam breaking problem. Other findings are very similar to the previous test case. That is, the results of XFEM and sXFEM are comparable and the performance of the iterative solver is better with sXFEM. However, the overall differences between XFEM and sXFEM are small for the rising droplet problem.

6. Conclusion

In this work, new and existing approaches to improve the condition number for XFEM system matrices resulting from two-phase flow problems have been investigated. We introduced a new criterion for the blocking of enrichment degrees of freedom. This approach, while decently improving the iteration counts, has to be applied with care, as it influences the approximation

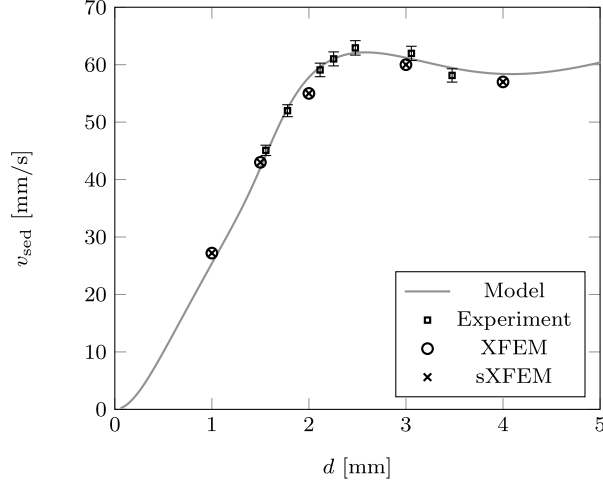


Figure 12: Rising droplet: Sedimentation velocity.

properties in a negative way. Diagonal scaling of the system matrix can be applied without hesitation and the authors advise to apply this approach on a general basis. Condition numbers of the scaled XFEM system matrix can be in the same order as of a corresponding standard FEM problem. The recently proposed stable XFEM provides a significant improvement of the iterative solver performance compared to standard XFEM. Additionally, using diagonal scaling with sXFEM further improves the performance. We showed that sXFEM and XFEM provide the same approximation properties for jumps in the solution. However, sXFEM is not able to accurately account for additional jumps in the solution *gradient*, in contrast to the sign-enrichment with standard XFEM. For two industrially relevant 3D two-phase/free-surface flow problems, we showed that the combination of diagonal scaling and blocking of degrees of freedom for XFEM can still be a great challenge for iterative solvers in extreme cases. sXFEM on the other side showed much better iterative solver performance in this case and the accuracy of the results seems comparable to those of the XFEM. We conclude that sXFEM is a promising approach to build an efficient and accurate two-phase flow solver. Nevertheless, the approximation properties and possible improvements of sXFEM still have to be investigated in more depth.

7. Acknowledgement

The authors gratefully acknowledge the computing resources provided by the AICES graduate school and RWTH Aachen University Center for Computing and Communication. The authors also wish to acknowledge the support of the German Science Foundation in the frame of the Emmy-Noether-research group “Numerical methods for discontinuities in continuum mechanics”.

References

- [1] M. Sussman, P. Smereka, S. Osher, A level set approach for computing solutions to incompressible two-phase flow, *J. Comput. Phys.* 114 (1994) 146 – 159.
- [2] C. Hirt, B. Nichols, Volume of fluid (VOF) method for the dynamics of free boundaries, *J. Comput. Phys.* 39 (1981) 201 – 225.
- [3] T. Tezduyar, M. Behr, J. Liou, A new strategy for finite element computations involving moving boundaries and interfaces - the deforming-spatial-domain/space-time procedure: II. Computation of free-surface flows, two-liquid flows, and flows with drifting cylinders, *Comput. Meth. Appl. Mech. Eng.* 94 (1992) 353 – 371.
- [4] A. H. Coppola-Owen, R. Codina, Improving eulerian two-phase flow finite element approximation with discontinuous gradient pressure shape functions, *Int. J. Numer. Meth. Fluid* 49 (2005) 1287 – 1304.
- [5] T. Belytschko, T. Black, Elastic crack growth in finite elements with minimal remeshing, *Int. J. Numer. Meth. Eng.* 45 (1999) 601 – 620.
- [6] N. Moës, J. Dolbow, T. Belytschko, A finite element method for crack growth without remeshing, *Int. J. Numer. Meth. Eng.* 46 (1999) 131 – 150.
- [7] J. Chessa, T. Belytschko, An extended finite element method for two-phase fluids, *J. Appl. Mech.* 70 (2003) 10 – 17.
- [8] J. Chessa, T. Belytschko, An enriched finite element method and level sets for axisymmetric two-phase flow with surface tension, *Int. J. Numer. Meth. Eng.* 58 (2003) 2041 – 2064.

- [9] S. Groß, A. Reusken, An extended pressure finite element space for two-phase incompressible flows with surface tension, *J. Comput. Phys.* 224 (2007) 40 – 58.
- [10] A. Kölke, Modellierung und Diskretisierung bewegter Diskontinuitäten in randgekoppelten Mehrfeldsystemen, Dissertation, Technische Universität Braunschweig (2005).
- [11] T. Fries, The intrinsic XFEM for two-fluid flows, *Int. J. Numer. Meth. Fluid* 60 (2008) 437 – 471.
- [12] P. Minev, T. Chen, K. Nandakumar, A finite element technique for multifluid incompressible flow using eulerian grids, *J. Comput. Phys.* 187 (2003) 255 – 273.
- [13] S. Zlotnik, P. Díez, Hierarchical X-FEM for n -phase flow ($n > 2$), *Comput. Meth. Appl. Mech. Eng.* 198 (2009) 2329 – 2338.
- [14] G. Legrain, N. Moës, A. Huerta, Stability of incompressible formulations enriched with X-FEM, *Comput. Meth. Appl. Mech. Eng.* 197 (2008) 1835 – 1849.
- [15] H. Sauerland, T.-P. Fries, The extended finite element method for two-phase and free-surface flows: A systematic study, *J. Comput. Phys.* 230 (2011) 3369 – 3390.
- [16] T. Fries, T. Belytschko, The extended/generalized finite element method: An overview of the method and its applications, *Int. J. Numer. Meth. Eng.* 84 (3) (2010) 253 – 304.
- [17] I. Babuska, U. Banerjee, Stable generalized finite element method (SGFEM), *Comput. Meth. Appl. Mech. Eng.* 201-204 (2012) 91 – 111.
- [18] A. Reusken, Analysis of an extended pressure finite element space for two-phase incompressible flows, *Comput. Visual Sci.* 11 (2008) 293 – 305.
- [19] E. Béchet, H. Minnebo, N. Moës, B. Burgardt, Improved implementation and robustness study of the X-FEM for stress analysis around cracks, *Int. J. Numer. Meth. Eng.* 64 (8) (2005) 1033 – 1056.

- [20] A. Menk, S. P. A. Bordas, A robust preconditioning technique for the extended finite element method, *Int. J. Numer. Meth. Eng.* 85 (13) (2011) 1609 – 1632.
- [21] Y. J. Choi, Modeling particulate complex flows using xfem, Ph.D. thesis, Technische Universiteit Eindhoven, Eindhoven (2011).
- [22] R. Croce, M. Griebel, M. A. Schweitzer, Numerical simulation of bubble and droplet deformation by a level set approach with surface tension in three dimensions, *Int. J. Numer. Meth. Fluid* 62 (9) (2009) 963 – 993.
- [23] T. Fries, A. Zilian, On time integration in the XFEM, *Int. J. Numer. Meth. Eng.* 79 (2009) 69 – 93.
- [24] F. Shakib, T. Hughes, Z. Johan, A new finite element formulation for computational fluid dynamics: X. The compressible Euler and Navier-Stokes equations, *Comput. Meth. Appl. Mech. Eng.* 89 (1991) 141 – 219.
- [25] S. Mittal, On the performance of high aspect ratio elements for incompressible flows, *Comput. Meth. Appl. Mech. Eng.* 188 (1-3) (2000) 269 – 287.
- [26] T. E. Tezduyar, Computation of moving boundaries and interfaces and stabilization parameters, *Int. J. Numer. Meth. Fluid* 43 (5) (2003) 555 – 575.
- [27] M. Kang, R. P. Fedkiw, X.-D. Liu, A boundary condition capturing method for multiphase incompressible flow, *J. Sci. Comput.* 15 (2000) 323 – 360.
- [28] S. Ganesan, G. Matthies, L. Tobiska, On spurious velocities in incompressible flow problems with interfaces, *Comput. Meth. Appl. Mech. Eng.* 196 (7) (2007) 1193 – 1202.
- [29] T. Belytschko, N. Moës, S. Usui, C. Parimi, Arbitrary discontinuities in finite elements, *Int. J. Numer. Meth. Eng.* 50 (2001) 993 – 1013.
- [30] J. Chessa, H. Wang, T. Belytschko, On the construction of blending elements for local partition of unity enriched finite elements, *Int. J. Numer. Meth. Eng.* 57 (2003) 1015 – 1038.

- [31] T. Fries, A corrected XFEM approximation without problems in blending elements, *Int. J. Numer. Meth. Eng.* 75 (2008) 503 – 532.
- [32] S. Balay, J. Brown, K. Buschelman, W. D. Gropp, D. Kaushik, M. G. Knepley, L. C. McInnes, B. F. Smith, H. Zhang, PETSc Web page, <http://www.mcs.anl.gov/petsc> (2011).
- [33] O. Axelsson, *Iterative solution methods*, Cambridge University Press, Cambridge, 1994.
- [34] P. Wriggers, *Nonlinear finite element methods*, 1st Edition, Springer Berlin Heidelberg, New York, NY, 2008.
- [35] R. F. Ausas, G. C. Buscaglia, S. R. Idelsohn, A new enrichment space for the treatment of discontinuous pressures in multi-fluid flows, *Int. J. Numer. Meth. Fluid* (2011) doi:10.1002/fld.2713.
- [36] P. E. Raad, R. Bidoae, The three-dimensional eulerian-lagrangian marker and micro cell method for the simulation of free surface flows, *J. Comput. Phys.* 203 (2005) 668 – 699.
- [37] K. W. Cheng, T.-P. Fries, XFEM with hanging nodes for two-phase incompressible flow, *Comput. Meth. Appl. Mech. Eng.* (2012) submitted.
- [38] E. Bertakis, S. Groß, J. Grande, O. Fortmeier, A. Reusken, A. Pfennig, Validated simulation of droplet sedimentation with finite-element and level-set methods, *Chem. Eng. Sci.* 65 (6) (2010) 2037 – 2051.